EDGE ARTICLE

Check for updates

All publication charges for this article have been paid for by the Royal Society of Chemistry

Surface reconstruction driven by low oxygen chemical potential sintering: unlocking superior material properties

Shuai Zhang,[a] Jiexi Wang, [ID abcd] Zhengwei Xu,[a] Muzhou Li,[a] Zhixing Wang, [ID abcd] Huajun Guo, [ID abcd] Xinhai Li, [ID abcd] Wenjie Peng,[abcd] Hui Duan, [ID a] Guangchao Li[a] and Guochun Yan [ID *abcd]

O3-Type layered oxides are promising Na-ion battery cathodes owing to their high theoretical capacity and facile synthesis. Increasing the upper cutoff voltage (V > 4.0 V *vs.* Na$^+$/Na) is crucial for improving the practical capacity. However, irreversible electrolyte side reactions at high voltages impede their practical applications. In this work, we develop a low oxygen chemical potential (LOCP) sintering strategy to modify the O3-type cathode, creating Ti-rich surfaces through structural reorganization. This surface engineering significantly enhances the interfacial stability between the cathode and the electrolyte, and the optimized cathode delivers an initial discharge capacity of 146.7 mA h g^{-1} with 85.6% capacity retention after 500 cycles in a pouch full-cell. Mechanistic studies reveal that LOCP sintering induces surface oxygen vacancies while enabling Na deintercalation and surface sodium residual accumulation. These oxygen vacancies promote bulk-to-surface Ti migration alongside Mn valence reduction, ultimately driving structural phase transitions. DFT calculations confirm that oxygen vacancies reduce Ti migration barriers, elucidating the atomic-scale transformation mechanism. This work sheds light on surface engineering of O3-type layered oxides and provides valuable insights for developing high-voltage sodium-ion batteries with extended cyclability.

Introduction

Na-ion batteries (NIBs) present promising prospects for the energy storage market, attributed to their cost-effectiveness and the availability of abundant raw materials.[1] Among various cathode materials for NIBs, O3-type layered oxides stand out for industrial applications owing to their ease of synthesis and high theoretical specific capacity.[2] However, to fully realize the potential of these materials, it is necessary to increase the charging cutoff voltage of the battery system. At high voltages, irreversible phase transitions occurring in the cathode material and the oxidative degradation of electrolyte lead to severe capacity decay.[3,4] Addressing these interfacial instability issues is essential for advancing the commercialization of NIBs.

Under high voltage conditions (≥4.2 V, V *vs.* Na$^+$/Na), the interface between O3-type cathodes and conventional electrolytes become thermodynamically unstable. The widely used carbonate-based electrolytes with NaClO$_4$ or NaPF$_6$ salt undergo decomposition at elevated potentials, forming an insulating surface layer that hinders ionic transport.[5,6] Concurrently, oxygen release and transition metal dissolution triggered by interfacial side reactions further exacerbate material's structural degradation.[7–9] These intertwined challenges underscore the urgency to develop cathode materials with enhanced interfacial stability for high-voltage NIB operation.

Surface coating has been widely explored as a primary strategy to mitigate interfacial degradation in layered oxide cathode materials. Current coating materials, including oxides,[10,11] metal fluorides,[12] phosphates,[13] and fast ion conductors,[14,15] aim to create a protective surface layer, which enhances the interfacial stability of the cathode. While effective in principle, practical implementation faces substantial hurdles in achieving uniform coating morphology with precise control over thickness and composition. This limitation motivates the search for alternative interfacial engineering approaches that combine process simplicity with performance reliability.

In this study, we propose a low oxygen chemical potential (LOCP) sintering strategy to *in situ* construct a stabilized interface on the NaNi$_{0.35}$Fe$_{0.2}$Mn$_{0.3}$Cu$_{0.05}$Ti$_{0.1}$O$_2$ (NFMCT) O3-type cathode material. While similar approaches have been previously reported for P2-type cathode materials,[16–18] application to

aSchool of Metallurgy and Environment, Central South University, Changsha 410083, China. E-mail: happyygc@csu.edu.cn

bEngineering Research Center of the Ministry of Education for Advanced Battery Materials, Central South University, Changsha 410083, China

cHunan Provincial Key Laboratory of Nonferrous Value-Added Metallurgy, Central South University, Changsha 410083, China

dNational Energy Metal Resources and New Materials Key Laboratory, Central South University, Changsha 410083, China

O3-type cathode remains underexplored. However, owing to the pronounced differences in sodium stoichiometry and crystal symmetry, P2 ($P6_3/mmc$) versus O3 ($R\bar{3}m$), identical LOCP protocols can drive fundamentally different structural and interfacial evolution pathways. Accordingly, elucidating the LOCP-driven evolution in O3-type cathode is necessary and timely. Here, by carefully controlling the calcination conditions at 600 °C under a low oxygen chemical potential, we synthesized the Ar-600 sample, which exhibits a distinct Ti-enriched and Mn-depleted surface phase transition layer. This structural feature was confirmed by scanning transmission electron microscopy and electron energy loss spectroscopy. Complementary characterization techniques, including electron paramagnetic resonance, surface residual alkali analysis, and open-circuit voltage measurements, collectively reveal the formation mechanism of this self-stabilized interface. Electrochemical evaluations in half-cell, full-cell, and pouch-cell configurations demonstrate significantly improved cycling stability for the Ar-600 sample as compared to untreated NFMCT. Further investigation through X-ray photoelectron spectroscopy, high-temperature self-discharge tests, and electrochemical impedance spectroscopy confirms enhanced interfacial stability and superior sodium-ion diffusion kinetics in the modified material. Density functional theory calculations provide atomic-level insights into the critical role of oxygen vacancies generated during low oxygen chemical potential sintering in regulating Ti migration and interface formation. This work establishes a novel material processing paradigm for engineering stable interfaces in layered oxide cathodes, offering a viable pathway toward high-performance NIBs.

Results and discussion

The NaNi$_{0.35}$Fe$_{0.2}$Mn$_{0.3}$Cu$_{0.05}$Ti$_{0.1}$O$_2$ (NFMCT) cathode material was synthesized via a conventional solid-state method, which was then subjected to secondary annealing in an LOCP environment at 400 °C, 600 °C, and 800 °C (denoted as Ar-400, Ar-600, and Ar-800, respectively). The XRD patterns confirm that all samples are indexed to the structure of O3-type cathode materials with the $R\bar{3}m$ space group (SI Fig. 1). It indicates that the LOCP treatment does not alter the structure of the O3-type NFMCT cathode material. The scanning electron microscopy (SEM) images (SI Fig. 2) demonstrate that both pre-LOCP and post-LOCP treatment samples exhibit single-crystal particle morphology, with an average particle size of 2–3 μm. Further EDS mapping reveals a uniform distribution of all elements on the surface of NFMCT and Ar-600 samples (SI Fig. 3 and SI Fig. 4), indicating that the LOCP treatment does not affect the characteristics of the uniform distribution of the elements at the micrometer level. Additionally, backscattered electron imaging in SEM confirms the absence of significant impurity phases of Ar-600 sample (SI Fig. 5), which is in accordance with the XRD analysis.

To grasp the structural features of the samples at the atomic level, the NFMCT and Ar-600 samples were treated using a focused ion beam (FIB) for scanning transmission electron microscopy (STEM) analysis. The cross-sectional atomic-resolution high-angle annular dark-field (HAADF) image of NFMCT (Fig. 1a) shows that the NFMCT exhibits a consistent atomic arrangement from the bulk phase to the surface, demonstrating that there is no phase transition and is well-crystallized. Fast Fourier transform (FFT) analysis of this region (Fig. 1d) reveals that the phase structure corresponds to the $R\bar{3}m$ space group with a [010] zone axis. These results confirm that the structure of NFMCT maintains homogeneity from the bulk to surface and retains the O3-type cathode structure. In contrast to NFMCT, the cross-sectional atomic HAADF-STEM image of the Ar-600 sample (Fig. 1b) shows structural variation on the surface. FFT analysis of the bulk and surface regions of the Ar-600 sample was performed to confirm the corresponding structure and zone axis orientation. In the bulk region (region f), the space group of this region is recognized as $R\bar{3}m$ with the zone axis [010] (Fig. 1f). Conversely, in the approximately 12 nm region near the surface (region e), the structure deviates from the $R\bar{3}m$ space group and recognized as the $C2/m$ space group with the [010] zone axis (Fig. 1e). This proves that LOCP treatment induces structural transformations on the surface region of NFMCT.

To further investigate the evolution of the $R\bar{3}m$ space group structure to the $C2/m$ space group structure, we analyze the atomic HAADF-STEM image of the middle region of the two phases for the Ar-600 sample, with pseudo-color coloring for convenience of observation (Fig. 1c). The image reveals a transition region (region III) between the surface (region II) and the bulk phase (region I), where there is a dislocation within the Na layer and transition metal (TM) layer. This indicates that the $R\bar{3}m$ structure first experienced dislocations between the Na and TM layers in the $R\bar{3}m$ space group, then formed the $C2/m$ space group structure, revealing the structural evolution process of layered oxide under LOCP treatment. Furthermore, the atomic HAADF-STEM image of the Ar-600 sample reveals that the brightness of the surface atomic columns is significantly lower than that of the bulk atomic columns, indicating that the average atomic mass of the surface atomic column elements is less than that of the bulk atomic columns.[16] This contrasts with the uniform atomic column brightness in the HAADF-STEM image for the NFMCT sample, indicating that the LOCP treatment induces the migration of elements at the surface of the material.

Inspired by the potential elemental migration from HAADF-STEM analysis, the electron energy loss spectroscopy (EELS) technique was employed to analyze the chemical state of surface elements of both the NFMCT and Ar-600 samples. The corresponding schematic diagrams of the EELS recording area and direction are presented in Fig. 2a and c. For NFMCT, the EELS spectra (Fig. 2b) reveal no evidence of oxygen vacancies or changes in elemental valence, corroborating the previously observed homogeneous surface structure. In contrast, the Ar-600 sample exhibits a weakening of the O pre-edge peak (indicated by the dashed line) of O K-edge from the bulk to the surface, with near-complete suppression at the outermost layer (Fig. 2d). As the pre-edge peak intensity is indicative of oxygen vacancies, this trend confirms the presence of oxygen vacancies within the top ~12 nm of the surface region.[16,19] Additionally,
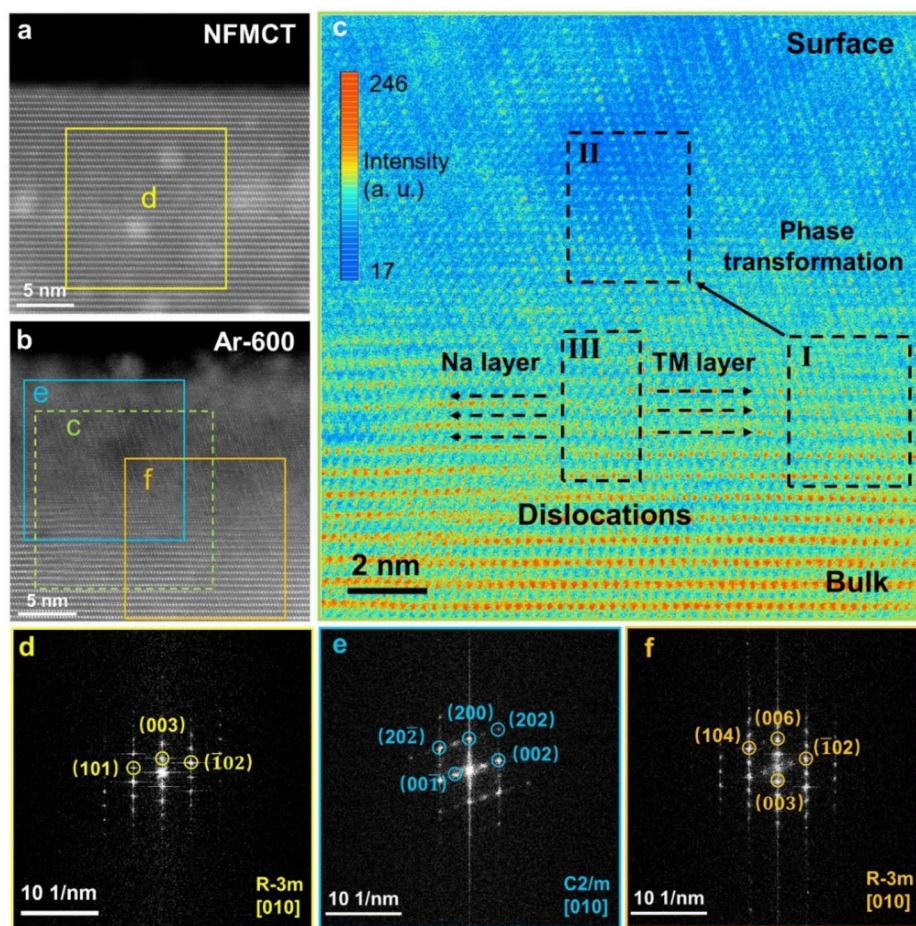
Fig. 1 Structural characterization of materials. (a) Atomic HAADF-STEM image of NFMCT. (b) Atomic HAADF-STEM image of Ar-600. (c) An enlarged view of the dashed region in (b) is shown in pseudo-color. (d) The FFT patterns of region d in (a, e and f). The FFT patterns of regions e and f in (b).

the Mn L-edge spectra of Ar-600 show a shift of the L3 and L2 peaks to lower energies near the surface, suggesting a reduction in Mn valence.[20] In contrast, the valence states of Ni, Fe, and Ti remain unchanged. These observations are absent in the NFMCT sample, where all elemental states remain consistent across the surface and bulk. Thus, the LOCP treatment results in a substantial increase in surface oxygen vacancies and a concurrent reduction in Mn valence, as indicated by the EELS analysis. To further validate the presence of oxygen vacancies, Electron Paramagnetic Resonance (EPR) spectroscopy was conducted (Fig. 2e). All samples exhibit a g-factor of 2.005, which is a signature of oxygen vacancies (SI Fig. 6).[21–23] Quantitative analysis (SI Table 1) shows that Ar-400 and Ar-600 have the highest and comparable concentrations of oxygen vacancies, while NFMCT and Ar-800 have significantly fewer oxygen vacancies. These results indicate that LOCP treatment at intermediate temperatures induces oxygen vacancies, primarily localized on the surface, as also confirmed by EELS. The correlation between reduced Mn valence and oxygen vacancy formation further supports the mechanism wherein oxygen anions donate electrons to Mn ions before escaping the lattice. The formation of these vacancies is driven by the difference in

the oxygen chemical potential between the bulk and the inert gas atmosphere. At elevated temperatures, oxygen diffuses from regions of high to low potential, which is facilitated by thermal energy.

However, for the Ar-800 sample, the vacancy concentration is comparable to that of the pristine NFMCT, in contrast to the higher levels observed in Ar-400 and Ar-600. This behavior can be attributed to a competing high-temperature process: under an inert atmosphere, Ni atoms in the layered oxide framework diffuse outward together with oxygen to form NiO impurities (SI Fig. 1) due to the higher thermodynamic stability of NiO at high temperatures.[24,25] In this case, Ni is removed from the bulk in the form of stable NiO, resulting in a lower net oxygen vacancy concentration despite the higher thermal energy available to promote vacancy generation.

EELS spectra were also used to map the distribution of elements from the surface inward. To reduce signal noise and improve reliability, multiple spectra were averaged and plotted as line profiles. For NFMCT (Fig. 2f and SI Fig. 7a), a uniform distribution of elements confirms its homogeneous surface. In contrast, Ar-600 (Fig. 2g and SI Fig. 7b) shows a gradient where Ti concentration decreases and Mn increases from the surface
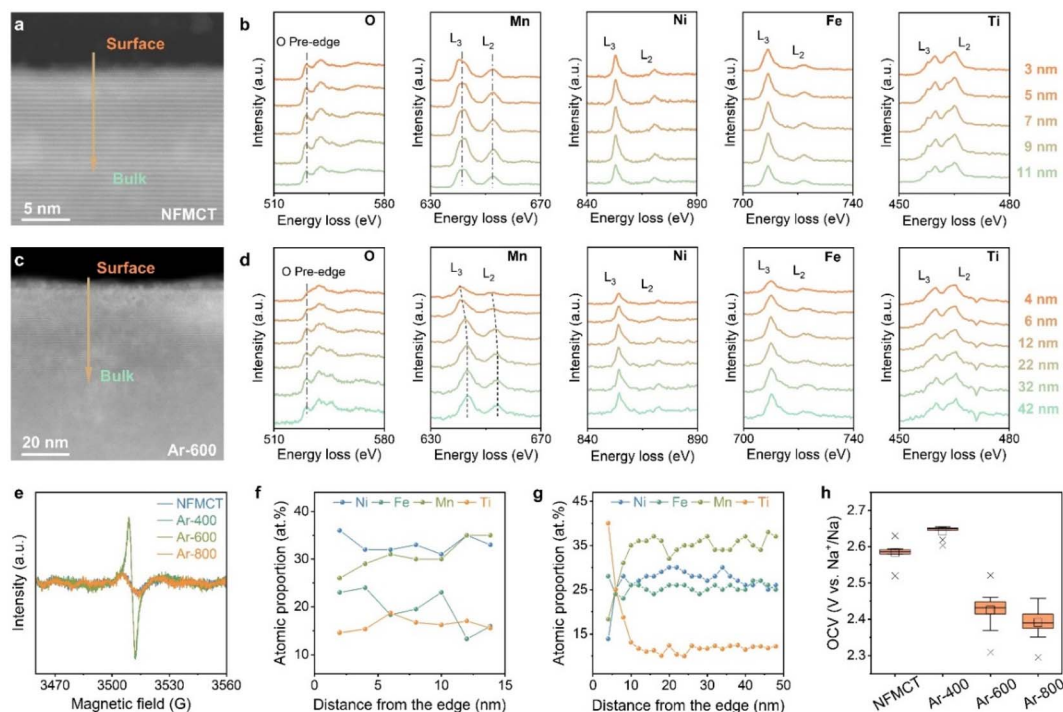
Fig. 2 Characterization of material surface states and oxygen vacancies. Schematic diagram of the area tested by EELS and the direction of the test for (a) NFMCT and (c) Ar-600. EELS spectra of (b) NFMCT and (d) Ar-600. (e) EPR spectra of NFMCT, Ar-400, Ar-600, and Ar-800. Distribution of the elemental content of (f) NFMCT and (g) Ar-600, analyzed by EELS characterization. (h) The open-circuit voltage of the coin half-cell for four samples.

to the bulk, while Ni and Fe remain unchanged. This indicates a Ti-rich, Mn-deficient surface, localized within the top ~12 nm, which is consistent with structural changes and oxygen vacancies. These results strongly suggest that LOCP treatment induces Ti migration to the surface, coupled with Mn valence changes and oxygen vacancy formation.

To assess the impact of Ti migration on the lattice structure, Rietveld refinement of XRD data was performed. All LOCP-treated samples exhibit reduced lattice parameters (a, b, and c) and volume (V) compared to NFMCT ($a = b = 2.984$ Å; $c = 16.026$ Å; $V = 123.58$ Å^3) (SI Fig. 8; SI Tables 2–5). While Ti doping in O3-type cathodes typically expands the lattice,[26–28] the observed contraction indicates Ti reduction from the bulk, consistent with its surface accumulation. Additionally, the Na layer spacing, d(O–Na–O), increases after LOCP treatment (SI Table 6), suggesting Na$^+$ deintercalation, which aligns with Na migration and Na$_2$CO$_3$ formation discussed below. Sodium migration during LOCP treatment was further examined by quantifying residual Na$_2$CO$_3$ on sample surfaces (SI Fig. 9 and Table 7). The Na content ($W_{(Na)}$) on NFMCT, Ar-400, Ar-600, and Ar-800 surfaces was 2871, 3801, 3408, and 3263 ppm, respectively, showing an initial increase followed by a decrease with increasing temperature. This trend suggests that oxygen vacancy formation promotes Na diffusion from the bulk to the surface, where it reacts with trace CO$_2$ in the chamber to form Na$_2$CO$_3$. Generally, an increase in the content of surface Na$_2$CO$_3$ is expected to increase the surface impedance and promote gas evolution during charge–discharge cycling. However, the

increments for Ar-400 (930 ppm) and Ar-600 (537 ppm) remain low compared with typical residual sodium levels in layered oxides, which is approximately 5000 to 10 000 ppm. Thus, this degree of carbonate accumulation is unlikely to exert a significant adverse impact on practical cell performance, which is further supported by the improved cycling stability observed for both Ar-400 and Ar-600 in subsequent electrochemical tests.

Based on the above integrated evidence, we propose the following mechanism for structural and chemical composition evolution in NFMCT under LOCP treatment. At elevated temperatures in the LOCP environment, surface oxygen atoms diffuse outward owing to the difference in oxygen chemical potentials, forming oxygen vacancies. Concurrently, Ti migrates from the bulk to the surface, Mn undergoes a valence state reduction, and Na$^+$ is extracted from the structure. These changes result in lattice distortion and a phase transition from the original $R\bar{3}m$ to a $C2/m$ structure, ultimately forming a Ti-enriched surface.

To validate this mechanism, we measured the open-circuit voltage (OCV) of half-cells assembled with the treated samples (Fig. 2h; 10 cells per each sample). OCV values initially increase and then decrease with increasing temperature. Since OCV is determined by the Fermi level difference between the cathode and anode, both the reduction in Mn^{4+} and formation of oxygen vacancies raise the cathode Fermi level, leading to a lower OCV.[29–32] For the Ar-400 sample, increased surface Na raises the OCV, akin to the charging process of a cell. In the Ar-600 sample, although less Na migrates to the surface, Mn valence

decreases significantly, elevating the Fermi level and lowering the OCV. In Ar-800, further reductions in surface Na slightly lower the OCV. These results corroborate the changes in Mn valence and Na distribution induced by LOCP treatment and support the proposed mechanism.

We further investigated the electrochemical properties of all samples using coin half-cells, with sodium metal as the negative electrode. The assembled cells were evaluated through a 0.1C charge–discharge test (Fig. 3a, and SI Table 8). The data demonstrate that LOCP treatment does not significantly affect the initial electrochemical characteristics, including specific capacity and coulombic efficiency. Then, we assessed the cycling stability of all samples at a current density of 1C (SI Fig. 10a). The results show that the cycling stability of the LOCP treated samples is enhanced, with the Ar-400 and Ar-600 samples exhibiting the improved performance. Notably, the Ar-600 sample maintains 80.2% of its initial capacity after 100 cycles. Additionally, the results of median voltage at 1C and the calculated energy density of all samples (Fig. 3b and SI Fig. 10b) demonstrate that LOCP treatment leads to an increase in median voltage and elevated energy density, particularly for the Ar-600 sample. Specifically, the initial energy density of the Ar-

600 sample reaches 520.9 W h kg^{-1} at 1C current density (calculated based on the mass of the cathode material). The Ar-800 sample shows slightly inferior performance compared with Ar-400 and Ar-600, which can be attributed to the presence of NiO impurities and the lower oxygen vacancy concentration, both of which hinder the formation of a robust surface reconstruction layer. And the assembled cells were further evaluated through galvanostatic measurements at various current densities (Fig. 3c). The data indicate that LOCP treatment does not affect the initial capacity at various current densities.

To evaluate the electrochemical performance of the samples more systematically, the performance of NFMCT and Ar-600 sample was further assessed using a coin full-cell, with hard carbon (HC) as the negative electrode (Fig. 3d–f and SI Table 9). The initial coulombic efficiency of the coin full-cells was approximately 85%, indicating a high level of efficiency and confirming successful full-cell matching. The cycling stability of NFMCT and Ar-600 sample was tested at 1C current density, with the Ar-600 sample showing 75.0% capacity retention after 300 cycles, while the NFMCT sample retained only 68.3%. This demonstrates that the Ar-600 sample exhibited superior cycling stability compared to NFMCT. A pouch full-cell using the Ar-600
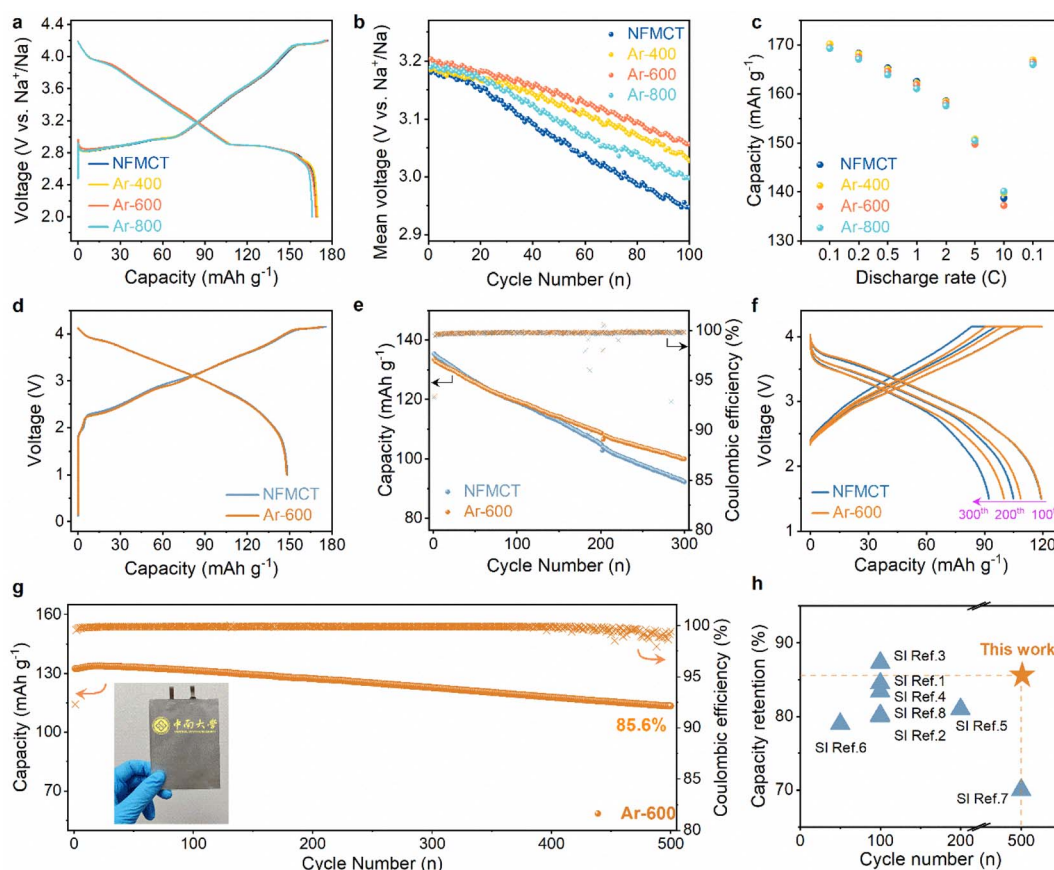
Fig. 3 Electrochemical performance of materials. (a) Initial charge–discharge curves of NFMCT, Ar-400, Ar-600, and Ar-800 at 0.1C with a coin half-cell. (b) Mean voltage decay plot for NFMCT, Ar-400, Ar-600, and Ar-800 at 1C with a coin half-cell. (c) Discharge specific capacity of NFMCT, Ar-400, Ar-600, and Ar-800 at different current densities. (d) Initial charge–discharge curves at 15 mA g^{-1} for a coin full-cell of NFMCT and Ar-600. (e) Cycling performance of a coin full-cell at 1C for NFMCT and Ar-600. (f) Charge–discharge curves at 150 mA g^{-1} for a coin full-cell of NFMCT and Ar-600. (g) Cycling performance of a pouch full-cell at 0.5C charging and 1C discharging for Ar-600. (h) Comparison of full-cell performance of O3-type cathode materials with the published literature (references are provided in the SI).

cathode (Fig. 3g and SI Table 9) was designed and assembled to further assess the performance of the Ar-600 sample.

The initial coulombic efficiency of the pouch full-cell was 86.3%, and the energy density was 465.6 W h kg^{-1} (based on the mass of the cathode material). The results of a long cycling test with 0.5C charging and 1C discharging demonstrate that it maintains a capacity retention of 85.6% after 500 cycles, which positions the full-cell among the top-performing cells reported in recent literature (Fig. 3h and SI Table 10). We further evaluated the Na$^+$ diffusion coefficients of NFMCT, Ar-400, Ar-600, and Ar-800 during both the charging and discharging processes using the galvanostatic intermittent titration technique (GITT) (SI Fig. 11). The results indicate that LOCP treatment does not significantly affect the Na$^+$ diffusion kinetics, suggesting that the reconstructed surface layer does not hinder Na$^+$ diffusion within the material.

To elucidate the effect of surface Ti enrichment on electrochemical performance, a series of surface characterization studies were conducted on aged electrodes from coin half-cells. X-ray photoelectron spectroscopy (XPS) was first employed to examine the surface states of NFMCT and Ar-600 samples at different states of charge (Fig. 4a and b). All spectra were calibrated using the C–C bond at 284.8 eV (SI Fig. 12). The O 1s spectra were divided into four components, corresponding to lattice oxygen, oxygenated inorganic species (e.g., Na$_2$CO$_3$ and Na$_2$O), organic electrolyte decomposition products (C–O and C=O), and Na-KLL Auger peaks.[33–35] To facilitate comparison, the peaks associated with oxygenated inorganic and organic species were normalized, and the relative proportion of electrolyte decomposition species was calculated. In the pristine state, both samples exhibited similar oxygen environments. However, after charging to 4.2 V, a distinct difference appeared
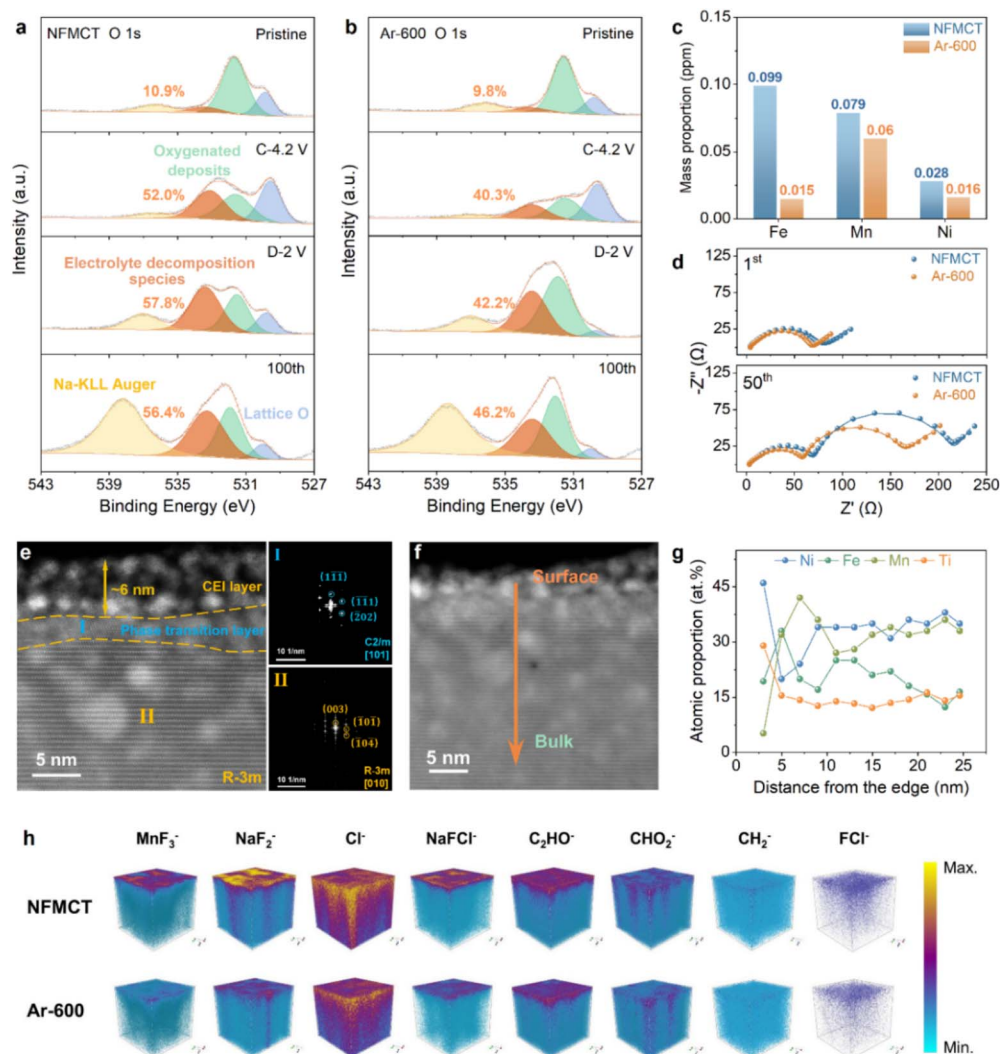

Fig. 4 Characterization of the effect of Ti elemental enrichment on surface properties. XPS spectra of O 1s in different states of the (a) NFMCT and (b) Ar-600 samples. (c) Transition metal element content in the sodium metal anode of NFMCT and Ar-600 half-cells after 100th aging. (d) EIS data and fitted data before and after cycling for NFMCT and Ar-600. (e) Atomic HAADF-STEM image of the Ar-600 sample after 100th cycling and the FFT patterns of regions I and II. (f) Schematic diagram of the area tested by EELS and the direction of the test for the Ar-600 sample after cycling. (g) Distribution of the elemental content for the Ar-600 sample after cycling, as analyzed by EELS characterization. (h) TOF-SIMS 3D visualization of NFMCT and Ar-600 electrodes (the samples were obtained after self-discharge measurement of the full cell).

in the intensity of the electrolyte decomposition peaks: NFMCT showed a significantly higher proportion (52%) than Ar-600 (40.3%), suggesting reduced electrolyte oxidation in the latter. This improvement is attributed to the Ti-rich surface and stable Ti–O bonds in the Ar-600 sample, which lower the presence of high-valence transition metals and suppress the oxidative side reactions. Further analysis of electrodes after full discharge (2.0 V) and after 100 cycles showed consistent results. Electrolyte decomposition products in NFMCT remained higher (57.8% and 56.4%) than in Ar-600 (42.2% and 46.2%), confirming that Ti surface enrichment mitigates electrolyte degradation throughout cycling. Moreover, the content of transition metal elements on the sodium metal anode of the aged battery was analyzed using Inductively Coupled Plasma Optical Emission Spectrometry (ICP-OES) (Fig. 4c). The NFMCT cell exhibited higher Fe, Mn and Ni levels, confirming that Ti surface enrichment in Ar-600 suppresses transition metal dissolution, contributing to enhanced electrode stability.

Ultimately, electrochemical impedance spectroscopy (EIS) was employed to characterize impedance changes in the NFMCT and Ar-600 samples before and after cycling, reflecting the surficial stability of cathode materials before and after LOCP treatment. The EIS spectra are illustrated in Fig. 4d, with the fitted data presented in SI Table 11, and the equivalent circuit diagram used for the fitting is displayed in SI Fig. 13. Pre-cycling EIS spectra were fitted with an equivalent circuit comprising electrolyte resistance (R_s) and charge transfer resistance (R_{ct}). After cycling, an additional resistance component attributed to the solid electrolyte interphase (R_{SEI}) was introduced. Initially, R_{ct} values were comparable between samples. Post-cycling, NFMCT exhibited higher R_{SEI} and R_{ct} (73.9 Ω and 132.5 Ω, respectively) compared to Ar-600 (60.6 Ω and 92.3 Ω), indicating less surface passivation and better Na^+ transport kinetics in the Ar-600 sample due to reduced interfacial side reactions.

The aforementioned results come to a solid conclusion that the as-obtained surface Ti-enriched Ar-600 sample through LOCP treatment displays superior interfacial stability during electrochemical cycling. To further confirm the structural stability of the surface Ti-enriched phase, Ar-600 samples after cycling were prepared using FIB and characterized via atomic-resolution HAADF-STEM and EELS (Fig. 4e–g and SI Fig. 14 and 15). HAADF-STEM revealed the persistence of a $C2/m$ phase transition layer within ~4 nm from the surface. EELS spectra confirmed Ti enrichment and the presence of oxygen vacancies in this region, while Mn remained in a reduced valence state. These findings verify the structural integrity and electrochemical stability of the Ti-enriched surface during cycling. Additionally, a cathode electrolyte interphase (CEI) layer with a thickness of approximately 6 nm is observed on the surface of the Ar-600 sample after cycling (Fig. 4e), compared to a significantly thicker ~12.5 nm CEI layer on the NFMCT sample (SI Fig. 16). The thickness of the CEI is correlated with the extent of electrolyte oxidative decomposition. The thinner CEI on the Ar-600 sample indicates fewer side reactions at the CEI, further confirming the improved interfacial stability resulting from the LOCP treatment.

To further validate the enhanced interfacial stability, self-discharge tests were conducted on coin full-cells at 100% SOC and 60 °C. Three identical cells per sample were tested, and the results are shown in SI Fig. 17. The Ar-600 cells exhibited significantly smaller voltage drops compared to NFMCT, confirming reduced self-discharge and superior electrode–electrolyte compatibility. Subsequently, we disassembled the self-discharged cell and then performed time-of-flight secondary ion mass spectrometry (TOF-SIMS) to analyze the ion species on the two cathode surfaces (Fig. 4h and SI Fig. 18). The TOF-SIMS results reveal significant differences in the surface decomposition products between NFMCT and Ar-600 measured in the same battery system. The detection of MnF_3^- ionic species on both samples indicates the dissolution and reaction of transition metals with the electrolyte system.[36] A higher abundance of MnF_3^- on the NFMCT sample suggests instability of the transition metals on the cathode surface in the electrolyte system.[37] Furthermore, other signals, including NaF_2^- and $NaFCl^-$ (arising from side reactions between F^-- and Cl^--containing species in the electrolyte with active Na), as well as Cl^-, C_2HO^-, CHO_2^-, CH_2^-, and FCl^- (from electrolyte decomposition products), are more prominent in the NFMCT sample compared to the Ar-600 sample. This suggests that the elemental enrichment of Ti on the surface of the Ar-600 sample mitigates these side reactions.[38]

The preceding characterization experiments, including XPS, TM dissolution analysis, EIS, TOF-SIMS, HAADF-STEM, EELS, and high-temperature self-discharge tests, collectively confirm that LOCP treatment enhances interfacial stability and cycling performance. These improvements are attributed to the enrichment of non-electrochemically active Ti elements and the stable Ti–O bond on the surface after LOCP treatment, which reduce the reactivity between electrochemically active elements and electrolyte, thus minimizing irreversible side reactions at the cathode surface. The stability of the surface phase transition layer after LOCP treatment was further confirmed by post-cycling characterization.

Although the enrichment of Ti on the surface and its role in enhancing interfacial stability have been established, the mechanism underlying the diffusion of Ti to the surface after LOCP treatment remains unclear. To uncover this, we performed Density Functional Theory (DFT) calculations to explore the thermodynamic and kinetic origins of Ti enrichment on the surface under LOCP. From a thermodynamic perspective, we first calculated the formation energies by constructing different surface reconstruction structures, which allowed determining which configuration is more stable. We began by calculating formation energies for four distinct models: (1) the original NFMCT model, corresponding to model 1 in Fig. 5a; (2) a model with two oxygen vacancies introduced into model 1 to calculate the formation energy with oxygen vacancies only, corresponding to model 2 in Fig. 5b; (3) a model in which the elemental ratios are modified based on previous EELS results for the surface region of the Ar-600 sample, with two oxygen vacancies introduced, as shown in model 3 in Fig. 5d; and (4) a model where we construct the $C2/m$ structure based on previous EELS and STEM results, modify the elemental ratio, and introduce
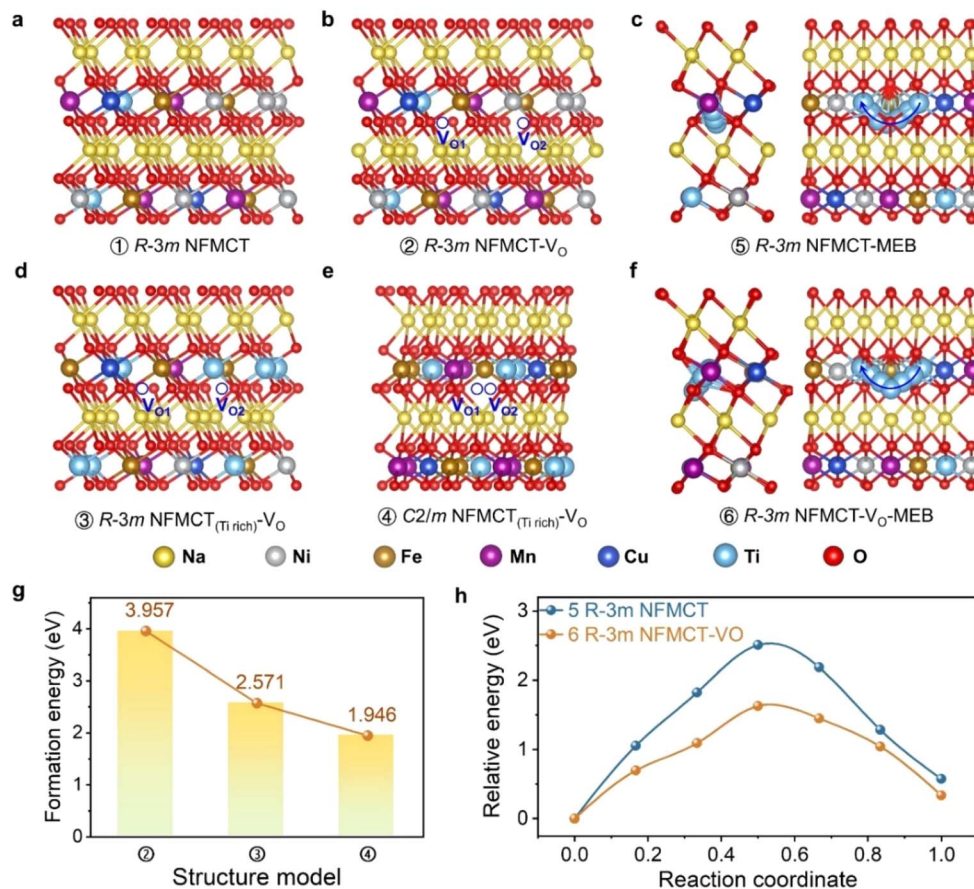
Fig. 5 DFT calculations of Ti elemental enrichment mechanism. (a) Formation energy calculations for the original crystal structure (Model 1; $R\bar{3}m$ space group, original atomic ratios, and no oxygen vacancies). (b) Introduction of two oxygen vacancies based on Model 1 (Model 2; $R\bar{3}m$ space group, original atomic ratio, and two oxygen vacancies). (c) Dual view of the Ti atom migration model for migration energy barrier calculations based on Model 1 (Model 5; $R\bar{3}m$ space group, no oxygen vacancies, and a migration path between two oxygen atoms). (d) Introduction of two oxygen vacancies into Model 1, with adjustments to elemental ratios according to Ti enrichment behavior (Model 3; $R\bar{3}m$ space group, elemental ratios adjusted according to EELS results, and two oxygen vacancies). (e) Introduction of two oxygen vacancies based on the $C2/m$ space group, with adjustments to elemental ratios according to Ti enrichment (Model 4; $C2/m$ space group, elemental ratios adjusted according to EELS results, and two oxygen vacancies). (f) Dual view of the Ti atom migration model for migration energy barrier calculations based on Model 1 with one oxygen vacancy (Model 6; $R\bar{3}m$ space group, one oxygen vacancy, and a migration path through the oxygen vacancy). The above model is a partial enlargement; a full view of the model is shown in the SI. (g) The formation energy of different models relative to Model 1. (h) The migration energy barrier for the two migration paths.

two oxygen vacancies, corresponding to model 4 in Fig. 5e. These models in the above graphs are partially enlarged pictures, and the corresponding complete model is shown in SI Fig. 19.

Based on the models described above, the formation energies of models 2, 3, and 4 relative to model 1 was calculated, and the results are presented in Fig. 5g. The formation energies, in descending order, are as follows: model 2 (3.957 eV), model 3 (2.571 eV), and model 4 (1.946 eV). These results suggest that the higher energy associated with the formation of oxygen vacancies in the NFMCT samples under LOCP is unfavorable for structural stability (model 2), causing the material to spontaneously transition toward a lower-energy configuration. The enrichment of Ti in surface regions with oxygen vacancies contributes to a decrease in the energy of the system (model 3). Additionally, the phase transition from $R\bar{3}m$ to $C2/m$ further reduces the energy of the system (model 4), resulting in a stable,

low-energy state. These findings, derived from DFT calculations, provide insight into the underlying mechanisms of oxygen vacancies driving the changes in element ratios on the surface and the structural transformation of the material after LOCP treatment.

In the above discussion, we calculated the formation energies of different reconstructed structures from a thermodynamic perspective and identified that the configuration with the $C2/m$ space group, oxygen vacancies, and Ti enrichment exhibits the lowest formation energy. However, the specific process through which Ti atoms enrich at the surface remains unclear. We therefore hypothesize that the presence of oxygen vacancies may reduce the migration energy barrier of Ti, thereby facilitating the diffusion of Ti atoms toward vacancy-rich surface regions. Further calculation of the migration energy barriers for Ti in the presence and absence of oxygen vacancies, corresponding to model 5 (Fig. 5c) and model 6 (Fig. 5f), was

performed. In the presence of oxygen vacancies, the migration path of Ti was designed to pass through the sites of oxygen vacancies. While in the absence of oxygen vacancies, Ti migration occurred between two oxygen atoms. The results of these migration energy barrier calculations (Fig. 5h) demonstrate that the migration energy barrier for Ti is significantly lower in the presence of oxygen vacancies compared to without oxygen vacancies, indicating that oxygen vacancies facilitate the migration and rearrangement of Ti. Collectively, the DFT analyses elucidate, from both thermodynamic and kinetic perspectives, the driving forces behind surface reconstruction after LOCP. Oxygen vacancies reduce the migration barrier, thereby promoting Ti diffusion to the surface. And the resulting Ti-enriched, $C2/m$-like reconstructed layer possesses a lower formation energy (thermodynamics), stabilizing the structure and promoting its development. These findings provide a coherent explanation for the elemental enrichment and structural transformation observed in NFMCT during LOCP sintering, thereby supporting our proposed hypothesis.

Conclusion

In this study, O3-type layered oxides were treated *via* low oxygen chemical potential (LOCP) sintering to induce surface reconstruction and enhance interfacial stability during electrochemical cycling. The LOCP treatment generated a Ti-rich surface with increased oxygen vacancy concentration, significantly suppressing interfacial side reactions with the electrolyte compared to the pristine sample. Mechanistic analysis revealed that under high-temperature LOCP conditions, oxygen escapes from the material surface, creating oxygen vacancies while triggering Na de-intercalation and surface sodium residual accumulation. Concurrently, Ti from the bulk phase migrates toward the oxygen vacancy-rich surface, coupled with Mn valence reduction. The synergistic effects oxygen vacancies and surface Ti enrichment drive the structural phase transition. We further validated this conclusion through Density Functional Theory (DFT) calculations, which confirmed that oxygen vacancies reduce Ti migration barriers, facilitating Ti enrichment in vacancy regions. The LOCP-treated cathode material (600 °C) demonstrated superior performance in pouch full-cells, achieving an initial coulombic efficiency of 86.3% and a capacity retention of 85.6% after 500 cycles. This strategy provides new insights into interfacial engineering of O3-type layered oxides for sodium-ion batteries and establishes a design framework for developing long-cycle-life secondary batteries.

Author contributions

Shuai Zhang and Guochun Yan conceived the idea and designed the experiments. Shuai Zhang conducted all experiments and associated analysis except ICP. Muzhou Li conducted the ICP test. Zhengwei Xu provided pouch full-cell support. Shuai Zhang and Guochun Yan wrote the manuscript. Jiexi Wang, Zhixing Wang, Huajun Guo, Xinhai Li, Wenjie Peng, Hui Duan and Guangchao Li supervised the work.

Conflicts of interest

Data availability

Acknowledgements

References

1 A. Rudola, R. Sayers, C. J. Wright and J. Barker, Opportunities for moderate-range electric vehicles using sustainable sodium-ion batteries, *Nat. Energy*, 2023, **8**, 215–218.

2 F. Ding, P. Ji, Z. Han, X. Hou, Y. Yang, Z. Hu, Y. Niu, Y. Liu, J. Zhang, X. Rong, Y. Lu, H. Mao, D. Su, L. Chen and Y.-S. Hu, Tailoring planar strain for robust structural stability in high-entropy layered sodium oxide cathode materials, *Nat. Energy*, 2024, **9**, 1529–1539.

3 G.-L. Xu, R. Amine, A. Abouimrane, H. Che, M. Dahbi, Z.-F. Ma, I. Saadoune, J. Alami, W. L. Mattis, F. Pan, Z. Chen and K. Amine, Challenges in Developing Electrodes, Electrolytes, and Diagnostics Tools to Understand and Advance Sodium-Ion Batteries, *Adv. Energy Mater.*, 2018, **8**, 1702403.

4 Y.-K. Sun, Direction for Commercialization of O3-Type Layered Cathodes for Sodium-Ion Batteries, *ACS Energy Lett.*, 2020, **5**, 1278–1280.

5 Y. You and A. Manthiram, Progress in High-Voltage Cathode Materials for Rechargeable Sodium-Ion Batteries, *Adv. Energy Mater.*, 2018, **8**, 1701785.

6 T. Song and E. Kendrick, Recent progress on strategies to improve the high-voltage stability of layered-oxide cathode materials for sodium-ion batteries, *J. Phys.: Mater.*, 2021, **4**, 032004.

7 Y. Huang, L. Zhao, L. Li, M. Xie, F. Wu and R. Chen, Electrolytes and Electrolyte/Electrode Interfaces in Sodium-

Ion Batteries: From Scientific Research to Practical Application, *Adv. Mater.*, 2019, **31**, 1808393.

8 B. Peng, G. Wan, N. Ahmad, L. Yu, X. Ma and G. Zhang, Recent Progress in the Emerging Modification Strategies for Layered Oxide Cathodes toward Practicable Sodium Ion Batteries, *Adv. Energy Mater.*, 2023, **13**, 2300334.

9 Q. Liu, Y.-H. Feng, X. Zhu, M. Liu, L. Yu, G.-X. Wei, X.-Y. Fan, X. Ji, P.-F. Wang and H. Xin, Stabilizing cathode-electrolyte interphase by localized high-concentration electrolytes for high-voltage sodium-ion batteries, *Nano Energy*, 2024, **123**, 109389.

10 J. Alvarado, C. Ma, S. Wang, K. Nguyen, M. Kodur and Y. S. Meng, Improvement of the Cathode Electrolyte Interphase on P2-Na2/3Ni1/3Mn2/3O2 by Atomic Layer Deposition, *ACS Appl. Mater. Interfaces*, 2017, **9**, 26518–26530.

11 Y. Yu, W. Kong, Q. Li, D. Ning, G. Schuck, G. Schumacher, C. Su and X. Liu, Understanding the Multiple Effects of TiO2 Coating on NaMn0.33Fe0.33Ni0.33O2 Cathode Material for Na-Ion Batteries, *ACS Appl. Energy Mater.*, 2020, **3**, 933–942.

12 H.-H. Sun, J.-Y. Hwang, C. S. Yoon, A. Heller and C. B. Mullins, Capacity Degradation Mechanism and Cycling Stability Enhancement of AlF3-Coated Nanorod Gradient Na[Ni0.65Co0.08Mn0.27]O2 Cathode for Sodium-Ion Batteries, *ACS Nano*, 2018, **12**, 12912–12922.

13 Y. Zhang, Y. Pei, W. Liu, S. Zhang, J. Xie, J. Xia, S. Nie, L. Liu and X. Wang, AlPO4-coated P2-type hexagonal Na0.7MnO2.05 as high stability cathode for sodium ion battery, *Chem. Eng. J.*, 2020, **382**, 122697.

14 Y. Li, Q. Shi, X. Yin, J. Wang, J. Wang, Y. Zhao and J. Zhang, Construction nasicon-type NaTi2(PO4)3 nanoshell on the surface of P2-type Na0.67Co0.2Mn0.8O2 cathode for superior room/low-temperature sodium storage, *Chem. Eng. J.*, 2020, **402**, 126181.

15 K. Tang, Y. Huang, X. Xie, S. Cao, L. Liu, M. Liu, Y. Huang, B. Chang, Z. Luo and X. Wang, The effects of dual modification on structure and performance of P2-type layered oxide cathode for sodium-ion batteries, *Chem. Eng. J.*, 2020, **384**, 123234.

16 J. Jin, Y. Liu, X. Zhao, H. Liu, S. Deng, Q. Shen, Y. Hou, H. Qi, X. Xing, L. Jiao and J. Chen, Annealing in Argon Universally Upgrades the Na-Storage Performance of Mn-Based Layered Oxide Cathodes by Creating Bulk Oxygen Vacancies, *Angew. Chem., Int. Ed.*, 2023, **62**, e202219230.

17 Y. Wang, Z. Sun, J. Jin, X. Zhao, X. Qu, L. Jiao and Y. Liu, In Situ Bulk Oxygen Vacancy Manufacturing and Surface Spinel Layer Coating Enable High-Performance Na-Ion Layered Fe–Mn Based Cathodes, *Adv. Funct. Mater.*, 2025, 2504354.

18 T. Ren, L.-K. Zhao, Z. Mei, H. Chen, Z.-M. Liu, X.-W. Gao, Q. Gu and W.-B. Luo, Constructing Oxygen Vacancy to Stable Anionic Redox Reaction for High Energy Sodium Battery, *Adv. Energy Mater.*, 2025, 2501007.

19 P. Yan, J. Zheng, J.-G. Zhang and C. Wang, Atomic Resolution Structural and Chemical Imaging Revealing the Sequential Migration of Ni, Co, and Mn upon the Battery Cycling of Layered Cathode, *Nano Lett.*, 2017, **17**, 3946–3951.

20 B. Cui, C. Song, F. Li, G. Y. Wang, H. J. Mao, J. J. Peng, F. Zeng and F. Pan, Tuning the entanglement between orbital reconstruction and charge transfer at a film surface, *Sci. Rep.*, 2014, **4**, 4206.

21 J. Xu, J. Wan, W. Zhang, Y. Li, F. Cheng, Z. Cheng, Y. Xu, S. Sun, Q. Li, C. Fang and J. Han, Regulating the Unhybridized O 2p Orbitals of High-Performance Li-Rich Mn-Based Layered Oxide Cathode by Gd-Doping Induced Bulk Oxygen Vacancies, *Adv. Funct. Mater.*, 2023, **33**, 2214613.

22 J. Chen, G. Zou, W. Deng, Z. Huang, X. Gao, C. Liu, S. Yin, H. Liu, X. Deng, Y. Tian, J. Li, C. Wang, D. Wang, H. Wu, L. Yang, H. Hou and X. Ji, Pseudo-Bonding and Electric-Field Harmony for Li-Rich Mn-Based Oxide Cathode, *Adv. Funct. Mater.*, 2020, **30**, 2004302.

23 S. Sun, X. Li, C. Zhang, X. Wang, J. Wang, C. Wang, Z. J. Xu, Z. Cheng and Y. Bai, Magnetic Field-induced Disordered Phase of Spinel Oxides for High Battery Performance, *Adv. Mater.*, 2024, **36**, 2405876.

24 S.-P. Lin, K.-Z. Fung, Y.-M. Hon and M.-H. Hon, Reaction Mechanism of LiNiO₂ Synthesized in Oxygen Atmosphere by Pechini Method, *J. Ceram. Soc. Jpn.*, 2002, **110**, 1038–1043.

25 R. Haugsrud, On the high-temperature oxidation of nickel, *Corros. Sci.*, 2003, **45**, 211–235.

26 W. Li, Y. Wang, G. Hu, Z. Peng, Y. Cao, Y. Zeng and K. Du, Ti-doped NaCrO2 as cathode materials for sodium-ion batteries with excellent long cycle life, *J. Alloys Compd.*, 2019, **779**, 147–155.

27 P.-F. Wang, H.-R. Yao, X.-Y. Liu, J.-N. Zhang, L. Gu, X.-Q. Yu, Y.-X. Yin and Y.-G. Guo, Ti-Substituted NaNi0.5Mn0.5-TiO2 Cathodes with Reversible O3−P3 Phase Transition for High-Performance Sodium-Ion Batteries, *Adv. Mater.*, 2017, **29**, 1700210.

28 Q. Wang, S. Mariyappan, J. Vergnet, A. M. Abakumov, G. Rousse, F. Rabuel, M. Chakir and J.-M. Tarascon, Reaching the Energy Density Limit of Layered O3-NaNi0.5Mn0.5O2 Electrodes via Dual Cu and Ti Substitution, *Adv. Energy Mater.*, 2019, **9**, 1901785.

29 G. Zhang, X. Wen, Y. Gao, R. Zhang and Y. Huang, Inhibiting Voltage Decay in Li-Rich Layered Oxide Cathode: From O3-Type to O2-Type Structural Design, *Nano-Micro Lett.*, 2024, **16**, 260.

30 J. B. Goodenough, Evolution of Strategies for Modern Rechargeable Batteries, *Acc. Chem. Res.*, 2013, **46**, 1053–1061.

31 S. Zhang, Z. Yang, Y. Lu, W. Xie, Z. Yan and J. Chen, Insights into Cation Migration and Intermixing in Advanced Cathode Materials for Lithium-Ion Batteries, *Adv. Energy Mater.*, 2024, **14**, 2402068.

32 E. Hu, X. Yu, R. Lin, X. Bi, J. Lu, S. Bak, K.-W. Nam, H. L. Xin, C. Jaye, D. A. Fischer, K. Amine and X.-Q. Yang, Evolution of redox couples in Li- and Mn-rich cathode materials and mitigation of voltage fade by reducing oxygen release, *Nat. Energy*, 2018, **3**, 690–698.

33 M. Sathiya, G. Rousse, K. Ramesha, C. P. Laisa, H. Vezin, M. T. Sougrati, M. L. Doublet, D. Foix, D. Gonbeau, W. Walker, A. S. Prakash, M. Ben Hassine, L. Dupont and J. M. Tarascon, Reversible anionic redox chemistry in high-

capacity layered-oxide electrodes, *Nat. Mater.*, 2013, **12**, 827–835.

34 T. Song, L. Chen, D. Gastol, B. Dong, J. F. Marco, F. Berry, P. Slater, D. Reed and E. Kendrick, High-Voltage Stabilization of O3-Type Layered Oxide for Sodium-Ion Batteries by Simultaneous Tin Dual Modification, *Chem. Mater.*, 2022, **34**, 4153–4165.

35 J.-C. Dupin, D. Gonbeau, P. Vinatier and A. Levasseur, Systematic XPS studies of metal oxides, hydroxides and peroxides, *Phys. Chem. Chem. Phys.*, 2000, **2**, 1319–1324.

36 F. Li, Z. Liu, C. Liao, X. Xu, M. Zhu and J. Liu, Gradient Boracic Polyanion Doping-Derived Surface Lattice Modulation of High-Voltage Ni-Rich Layered Cathodes for High-Energy-Density Li-Ion Batteries, *ACS Energy Lett.*, 2023, **8**, 4903–4914.

37 G.-T. Park, S.-B. Kim, B. Namkoong, J.-H. Ryu, J.-I. Yoon, N.-Y. Park, M.-C. Kim, S.-M. Han, F. Maglia and Y.-K. Sun, Intergranular Shielding for Ultrafine-Grained Mo-Doped Ni-Rich Li[Ni0.96Co0.04]O2 Cathode for Li-Ion Batteries with High Energy Density and Long Life, *Angew. Chem., Int. Ed.*, 2023, **62**, e202314480.

38 J. Li and A. Manthiram, A Comprehensive Analysis of the Interphasial and Structural Evolution over Long-Term Cycling of Ultrahigh-Nickel Cathodes in Lithium-Ion Batteries, *Adv. Energy Mater.*, 2019, **9**, 1902731.